Key Points:
- We measure shear wave splitting beneath southern Peru and northern Bolivia to constrain seismic anisotropy
- Evidence for contributions from the mantle wedge, subducting slab, and subslab mantle, with a weak contribution from the overriding plate
- Observations contradict predictions from simplest flow models and olivine fabric scenarios, suggesting complex mantle flow and deformation

Supporting Information:
- Supporting Information S1
- Table S1
- Table S2
- Table S3
- Table S4
- Table S5
- Table S6

Correspondence to:
M. D. Long,
maureen.long@yale.edu

Overriding plate, mantle wedge, slab, and subslab contributions to seismic anisotropy beneath the northern Central Andean Plateau

Maureen D. Long[1], C. Berk Biryol[2,3], Caroline M. Eakin[4,5], Susan L. Beck[2], Lara S. Wagner[6], George Zandt[2], Estella Minaya[7], and Hernando Tavera[8]

[1]Department of Geology and Geophysics, Yale University, New Haven, Connecticut, USA, [2]Department of Geosciences, University of Arizona, Tucson, Arizona, USA, [3]Department of Geological Sciences, University of North Carolina, Chapel Hill, North Carolina, USA, [4]School of Ocean and Earth Science, University of Southampton, Southampton, UK, [5]National Oceanography Centre Southampton, Southampton, UK, [6]Department of Terrestrial Magnetism, Carnegie Institution for Science, Washington, District of Columbia, USA, [7]Observatorio San Calixto, La Paz, Bolivia, [8]Instituto Geofísico del Perú, Lima, Peru

Abstract The Central Andean Plateau, the second-highest plateau on Earth, overlies the subduction of the Nazca Plate beneath the central portion of South America. The origin of the high topography remains poorly understood, and this puzzle is intimately tied to unanswered questions about processes in the upper mantle, including possible removal of the overriding plate lithosphere and interaction with the flow field that results from the driving forces associated with subduction. Observations of seismic anisotropy can provide important constraints on mantle flow geometry in subduction systems. The interpretation of seismic anisotropy measurements in subduction settings can be challenging, however, because different parts of the subduction system may contribute, including the overriding plate, the mantle wedge above the slab, the slab itself, and the deep upper mantle beneath the slab. Here we present measurements of shear wave splitting for core phases (*SKS, SKKS, PKS*, and *sSKS*), local *S*, and source-side teleseismic *S* phases that sample the upper mantle beneath southern Peru and northern Bolivia, relying mostly on data from the CAUGHT experiment. We find evidence for seismic anisotropy within most portions of the subduction system, although the overriding plate itself likely makes only a small contribution to the observed delay times. Average fast orientations generally trend roughly trench-parallel to trench-oblique, contradicting predictions from the simplest two-dimensional flow models and olivine fabric scenarios. Our measurements suggest complex, layered anisotropy beneath the northern portion of the Central Andean Plateau, with significant departures from a two-dimensional mantle flow regime.

1. Introduction

Continental subduction systems, in which a dense oceanic plate sinks beneath a relatively buoyant and thick continental overriding plate, represent a key tectonic setting on Earth. Continental subduction zones produce arc volcanism (and thus new crustal material) on the overriding plate, and often produce extensive zones of high topography. The Central Andean Plateau in the central part of the South American subduction zone, the second-highest plateau on Earth, is a particularly spectacular example of orogenesis in a continental subduction system [e.g., *Lamb and Hoke*, 1997]. While subduction zones are the locus for a number of important processes in the Earth's crust and upper mantle, their dynamics are a challenge to study, and differences in the characteristics of different subduction zones remain poorly understood. Again, the subduction of the Nazca Plate beneath South America is a fascinating example, both because of the impressive topography and because of pronounced along-strike and temporal variations in, for example, slab morphology and behavior, seismicity, volcanic character, overriding plate deformation, and topographic evolution [e.g., *Strecker et al.*, 2007; *Garzione et al.*, 2008; *Ramos and Folguera*, 2009; *Bilek*, 2010].

Seismic anisotropy, or the directional dependence of seismic wave speeds, is one observable that can help to constrain dynamic processes in subduction systems [e.g., *Savage*, 1999; *Long and Silver*, 2008; *Faccenda and Capitanio*, 2013; *Long*, 2013; *Di Leo et al.*, 2014]. A large number of studies of seismic anisotropy in

subduction zones have been carried out, yielding insight into mantle flow patterns, slab deformation, the transport of melt and volatiles in the mantle wedge, and the coupling between slabs and the surrounding upper mantle (for a recent overview, see *Long* [2013]). However, the interpretation of seismic anisotropy in subduction zones can be quite challenging, in large part because commonly used seismic phases sample a number of distinct portions of the subduction systems, including the overriding plate, the mantle wedge above the slab, the slab itself, and the subslab mantle. These difficulties have been particularly acute for the South American subduction region; although a large number of studies have been carried out [e.g., *Russo and Silver*, 1994; *Bock et al.*, 1998; *Polet et al.*, 2000; *Anderson et al.*, 2004; *MacDougall et al.*, 2012; *Hicks et al.*, 2012; *Eakin and Long*, 2013; *Porritt et al.*, 2014; *Wölbern et al.*, 2014; *Eakin et al.*, 2014, 2015], interpretations are often nonunique and hampered by complexities in observed splitting patterns and the likely presence of multiple layers of anisotropy at depth.

The approach that we take in this study is to simultaneously measure shear wave splitting (fast orientation ϕ and delay time δt) for three different types of seismic phases that sample different portions of the subduction system in different ways, allowing us to discriminate contributions from the overriding plate, the mantle wedge, the subducting slab, and the subslab mantle. Specifically, we measure the splitting of local *S* phases that originate from earthquakes at depths greater than ~100 km within the subducting slab itself, measured at stations located directly above the events. These phases sample the mantle wedge and the overriding plate, and measurement of phases originating from different depths allows us to estimate the likely strength and depth distribution of anisotropy within the wedge. We combine these measurements with core phases (*SKS, SKKS, PKS*, and *sSKS*; hereinafter **KS*) that sample all the way from the core-mantle boundary to the surface; these are thought to mostly reflect upper mantle anisotropy beneath the station, providing a path-integrated measure of splitting at all upper mantle depths and thus sampling multiple layers of the subduction system. Finally, we also include so-called source-side splitting measurements from direct teleseismic *S* phases that originate at earthquakes within the slab and are measured at distant stations; these phases mainly reflect anisotropy in the slab and the subslab mantle.

The focus of this study is the northern portion of the Central Andean Plateau (Figure 1), a region of particularly high topography that includes the ~4 km high Bolivian Altiplano [e.g., *Lamb and Hoke*, 1997]. Beneath our study area, the Nazca Plate is subducting beneath South America at a rate of 78 mm/yr with a convergence direction of approximately N75°E, according to the HS3-NUVEL1A plate motion model [*Gripp and Gordon*, 2002]. The age of the subducting lithosphere is ~50 Myr [*Heuret and Lallemand*, 2005] and the slab dip in the upper mantle is ~25° [*Syracuse and Abers*, 2006]. The trench is rolling back at a rate of approximately 35 mm/yr in a Pacific hotspot reference frame [*Heuret and Lallemand*, 2005], although the magnitude and direction of trench migration varies depending on the reference frame choice [e.g., *Schellart et al.*, 2008]. The overriding plate in our study area is in strong compression [e.g., *Heuret and Lallemand*, 2005]. Our study region encompasses the northern portion of the Bolivian Orocline, which corresponds to a marked curvature of the Andes and a change in the strike of the trench (Figure 1 inset). Finally, our study area is located just to the south and east of the Peruvian flat slab segment and the subducting Nazca Ridge on the downgoing plate [e.g., *Cahill and Isacks*, 1992; *Hampel*, 2002; *Rosenbaum et al.*, 2005; *Phillips and Clayton*, 2014; *Antonijevic et al.*, 2015].

We mostly rely on data from the 50 station broadband array called CAUGHT (Central Andes Uplift and Geodynamics of High Topography), which was deployed between 2010 and 2012 in southern Peru and northern Bolivia. This deployment of seismometers was part of a multidisciplinary effort to test geodynamic models for surface uplift, deformation history, and lithospheric evolution in this region (http://www.sas.rochester.edu/ees/SIREAL/CAUGHTwebsite/CAUGHT.html). There are major outstanding questions about the timing of topographic change, the mechanisms for crustal shortening and thickening, the presence or absence of a dense crustal root, the extent and mechanisms for lithospheric removal, and the pattern of flow in the mantle wedge and its effects on the overriding plate. Just to the north of the CAUGHT study region, a complementary seismic experiment known as PULSE was deployed over the southern portion of the Peruvian flat slab between 2010 and 2013. The along-strike transition from flat to normal subduction near our study area likely affects many aspects of subduction zone behavior, potentially including the anisotropic structure [e.g., *Eakin et al.*, 2014, 2015].

Here we present a set of 640 local *S* splitting measurements, 430 **KS* splitting measurements, and 20 source-side teleseismic *S* measurements that sample the portion of the Nazca subducton system between
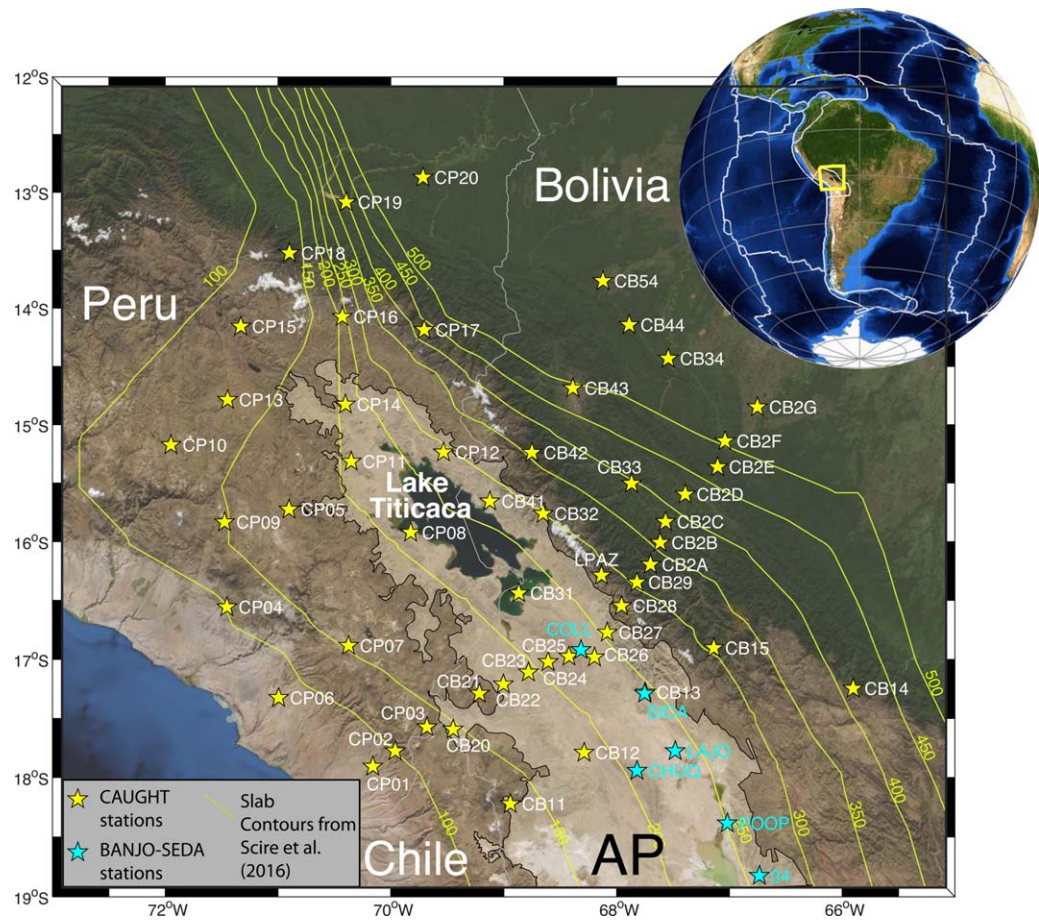
Figure 1. Station map and geographic setting. Locations of CAUGHT stations (yellow stars) are shown on top of a satellite image of southern Peru and northern Bolivia. Stations of the previous BANJO experiment are shown with blue stars. Red lines indicate slab contours at depth from the model of *Scire et al.* [2016]. Light-shaded region outlines the Central Andean Plateau (AP); Lake Titicaca is visible at the northern end of the plateau (blue region). Inset shows the location of the study area, on the western boundary of the South American plate.

13.5° and 18.5°S. We find evidence for significant anisotropy within and beneath the subducting Nazca plate, with somewhat weaker anisotropy in the mantle wedge and overriding plate above the slab. Overall, our measurements argue for significant complexity in anisotropic structure beneath the CAUGHT study area, with distinct contributions from many individual portions of the subduction system.

2. Data and Methods

2.1. *KS Splitting

We used data from the 50 stations of the CAUGHT array (Figure 1), recorded between late 2010 and mid-2012. We also examined data from station LPAZ of the Global Telemetered Seismograph Network, located in La Paz, Bolivia, from the same time period. We searched for candidate earthquakes of magnitude 5.8 or greater at epicentral distances between 90° and 150°. Data were bandpass filtered between 0.02 and 1 Hz; in a small minority of cases, the corner frequencies were adjusted manually to optimize waveform clarity. After filtering, we identified records with a clear core phase arrival with initial polarizations (estimated directly from the waveforms) within 10° of the backazimuth. We examined a number of different core phases including *SKS, SKKS, PKS,* and *sSKS* in order to maximize the number of measurements and the backazimuthal coverage. Phases other than *SKS* represent a significant portion (more than half) of the data set. A map of all earthquakes that yielded at least one splitting measurement is shown in Figure 2, and an example record section for an *SKS* arrival measured at CAUGHT stations in shown in Figure 3.
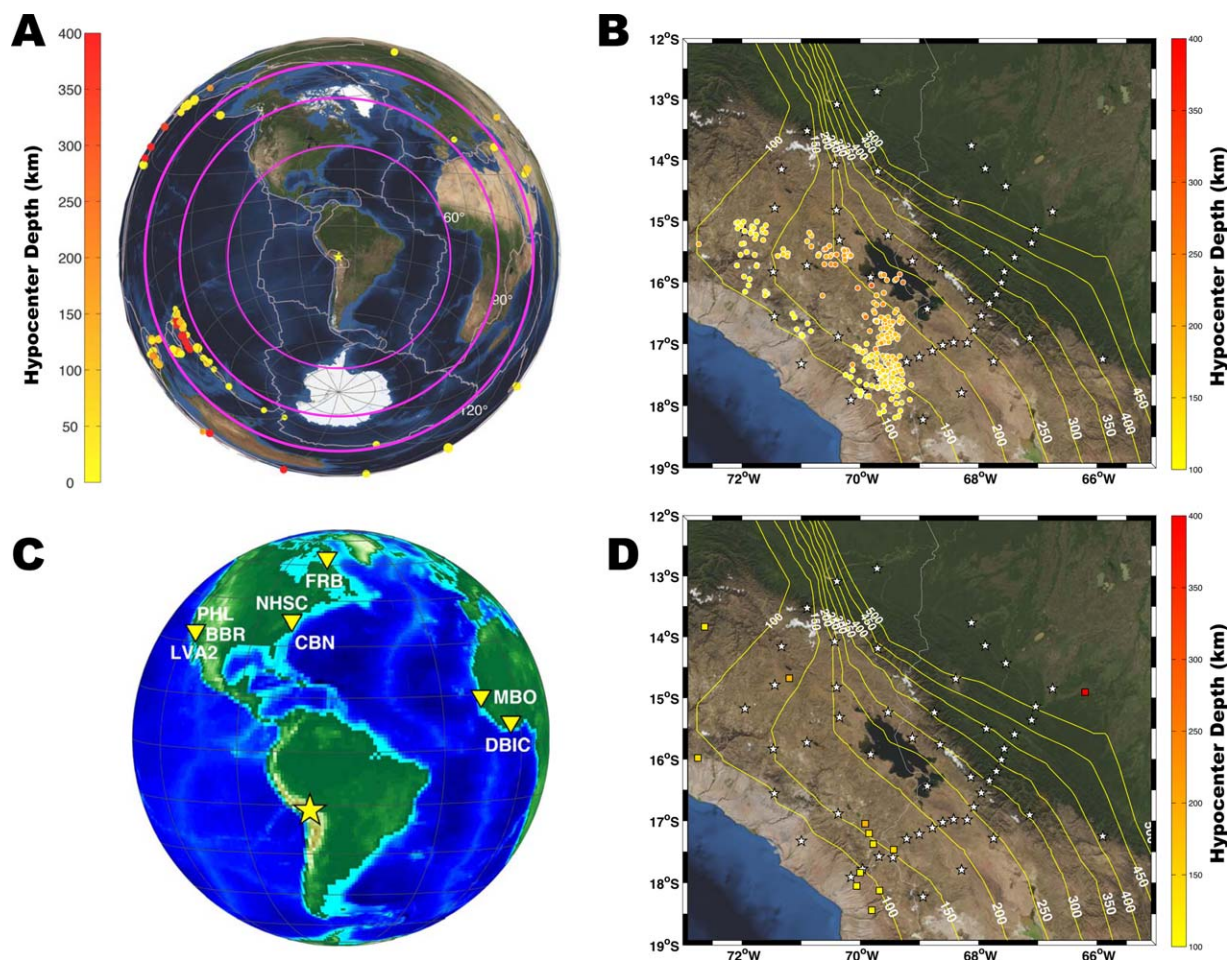
Figure 2. Earthquake locations and non-CAUGHT station locations. (a) Map of events used for *KS splitting analysis in this study. Each earthquake that yielded at least one usable measurement is shown with a dot; colors indicate event depth, as shown by the color bar. CAUGHT array location is shown with a star. Epicenter distances are indicated by pink dashed lines from 60° to 120°, in 30° increments. (b) Event map for local S. Circles indicate locations of slab earthquakes used for local S splitting measurements, color coded by event depth as shown by the color bar. Event locations from the catalogs of *Kumar et al.* [2016] and the Instituto Geofisico del Perú [see *Eakin et al.*, 2014] were used in this study. CAUGHT station locations are shown with red stars; thin red lines indicate slab contours from the model of *Scire et al.* [2016]. (c) Station locations for source-side teleseismic S measurements (yellow triangles); CAUGHT array location is shown with a star. (d) Events used for teleseismic source-side measurements (squares) color coded by event depth, as shown by the color bar. CAUGHT station locations are shown with stars.

We used the SplitLab software for analysis [*Wüstefeld et al.*, 2008] and simultaneously applied the transverse component minimization, rotation-correlation, and eigenvalue measurement methods to estimate the polarization of the fast quasi-S wave (fast orientation, ϕ) and delay time between the fast and slow arrivals (δt). In order to discriminate between null (i.e., nonsplit) and clearly split arrivals and assign an objective, quantitative assessment of measurement quality, we compared the splitting parameter estimates derived from the rotation-correlation method with those derived from the transverse component minimization method (also known as the *Silver and Chan* [1991] method), following *Wüstefeld and Bokelmann* [2007]. Specifically, we examined the difference in estimated fast orientation for the two methods for each arrival ($\phi_{RC} - \phi_{SC}$) as well as the ratio of the estimated delay times for the two methods ($\delta t_{RC}/\delta t_{SC}$), as shown in Figure 4. (This choice of measurement methods to compare follows *Wüstefeld and Bokelmann* [2007]; given the good resolution of splitting parameter estimates for measurements presented here, a comparison of the rotation-correlation and eigenvalue method would look similar.) For well-constrained split measurements, the two methods should yield similar fast orientations and delay times, while for well-constrained null arrivals, the difference in measured fast orientation $\phi_{RC} - \phi_{SC}$ should be close to 45° and $\delta t_{RC}/\delta t_{SC}$ should be close to zero [*Wüstefeld and Bokelmann*, 2007]. Null and nonnull measurements were assigned a "good" or "fair" quality based on how closely they conformed to these predictions, as illustrated in Figure 4 and as suggested by *Wüstefeld and Bokelmann* [2007].
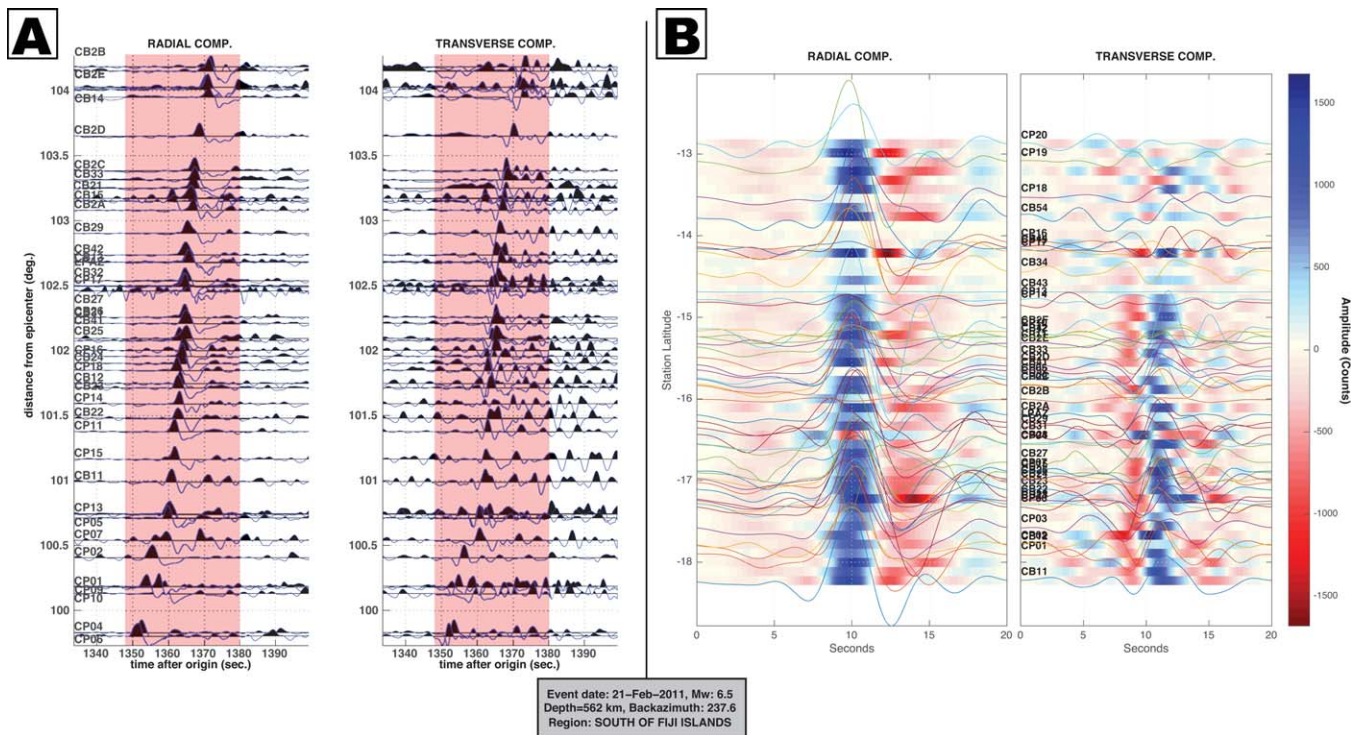
Figure 3. Example *SKS* record section for an event used in our **KS* splitting analysis. (a) Radial (left plot) and transverse (right plot) components for a deep (z = 562 km) earthquake in the Tonga-Fiji subduction zone on 21 February 2011. Traces are ordered by epicentral distance and have been filtered between 0.02 and 1 Hz. Pink box highlights the arrival of the *SKS* phase. Both components have been normalized by the maximum of each trace to emphasize the arrival. (b) Same data as in Figure 3a, but traces have been ordered by station latitude, from north (top) to south (bottom). Traces have been windowed around the *SKS* arrival and aligned on the expected *SKS* arrival time. Background colors indicate the actual amplitudes without normalization. This arrival clearly illustrates the generally weaker splitting (smaller transverse component amplitude) in the northern part of the array.

2.2. Local *S* Splitting

As with the **KS* analysis, our local *S* splitting analysis relied on data from CAUGHT stations plus permanent station LPAZ. We used two earthquake catalogs; the first is the catalog maintained by the Instituto Geofisico del Perú, which was also used for local *S* splitting analysis in southern Peru by Eakin et al. [2014]. This catalog was used for events shallower than 200 km. We also used the catalog developed using data from both CAUGHT and the contemporaneous PULSE deployment just to the north and west [*Kumar et al.*, 2016]; this catalog was used for events deeper than 200 km. We searched for events of magnitude 4 and greater at depths between 100 km and 250 km during the time period of deployment. Local *S* splitting analysis requires phases with steep incidence angles to avoid transverse component energy due to phase conversions near the free surface, so we searched for earthquakes at epicentral distances less than 1° from the station. A map of local earthquakes that yielded at least one good direct *S* splitting measurement is shown in Figure 2. Waveforms were initially bandpass filtered between 0.5 and 3 Hz (as local *S* arrivals have more high-frequency content than **KS* waves), but the filter parameters were manually adjusted to optimize waveform clarity for each arrival, with the high frequency cut-off ranging from 2 to 10 Hz. After filtering, records with clear, high amplitude direct *S* arrivals were selected for analysis.

As with the core phases, we used the SplitLab software to estimate splitting parameters, and simultaneously applied different measurement methods to ensure measurement quality. Because the initial polarization of direct *S* phases is controlled by the earthquake source, and not by a *P*-to-*S* conversion as for **KS* waves, we did not use the transverse component minimization method, and focused only on the rotation-correlation and eigenvalue methods. As with the **KS* measurements, we applied criteria based on the difference between measurement methods suggested by *Wüstefeld and Bokelmann* [2007] to assign quality ratings and discriminate between split and null arrivals (Figure 4). However, for direct *S* phases we examined the differences between splitting parameter estimates obtained using the rotation-correlation method and the eigenvalue method ($\phi_{RC} - \phi_{EV}$ and $\delta t_{RC}/\delta t_{EV}$).
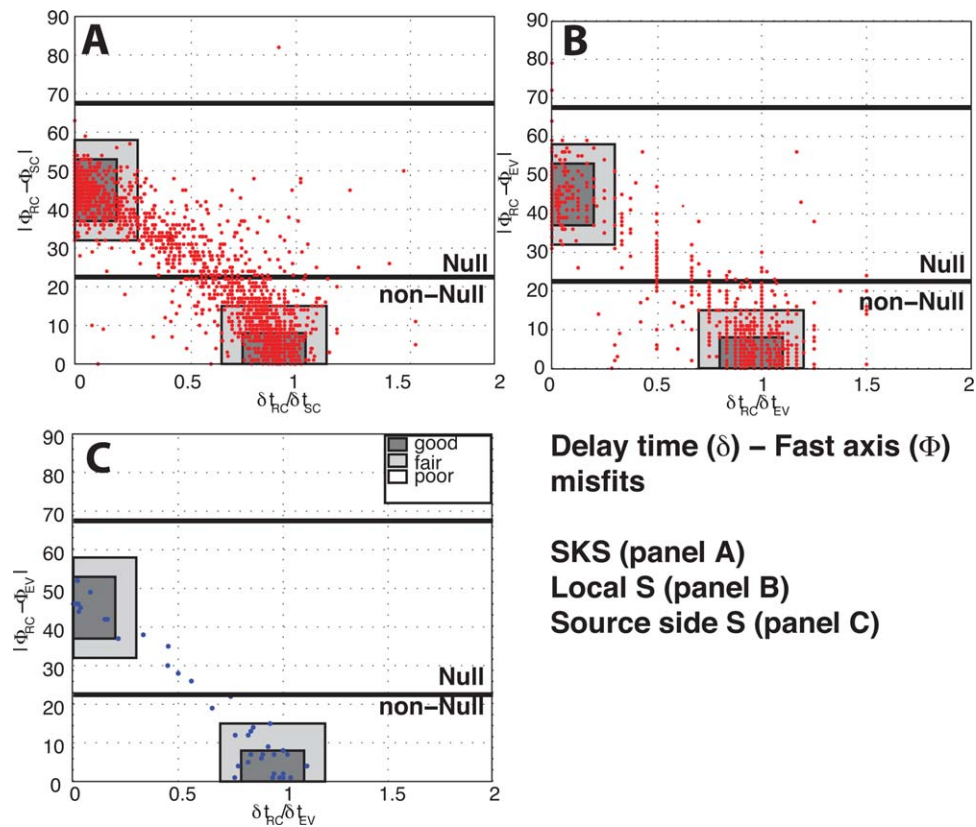
Figure 4. Plots indicating measurement quality for (a) *KS, (b) local S, and (c) source-side teleseismic S arrivals examined in this study. Each measurement is shown by a dot, with red dots indicating measurements made at CAUGHT stations and blue dots indicating measurements made at teleseismic stations. On each plot, x axis indicates the difference in shear wave splitting delay time (δt) measured by two measurement methods; y axis indicates the difference in fast orientation (ϕ) by the two methods. For *KS phases, we show the difference between the transverse component minimization (SC) and rotation-correlation (RC) methods; for local and teleseismic direct S, we use the eigenvalue (EV) and rotation-correlation (RC) methods. Shaded dark gray and light gray boxes indicate good and fair quality measurements, respectively, with a line dividing the space into null and non-null measurements, following *Wüstefeld and Bokelmann* [2007].

2.3. Source-Side Teleseismic S Splitting

In order to augment the set of splitting measurements obtained with the CAUGHT stations, we also analyzed the splitting of direct S phases originating from earthquakes within the subducting Nazca plate beneath the CAUGHT study area measured at distant stations. This measurement strategy, known as source-side splitting, has been extensively used to probe anisotropy in the deep upper mantle beneath subducting slabs, both in South America [*Russo and Silver*, 1994; *Eakin and Long*, 2013] and in other regions [e.g., *Russo*, 2009; *Lynner and Long*, 2013, 2014]. This technique constrains anisotropy in the upper mantle near the source by carrying out a correction for upper mantle anisotropy beneath the receiver and assuming that the lower mantle far away from subducting slabs (which may induce midmantle deformation) is generally isotropic. In order for this technique to reliably estimate the contribution from source-side anisotropy, it is necessary to use stations at which the upper mantle anisotropy signal is well-known and simple (i.e., consistent with apparent isotropy or a single horizontal layer of anisotropy), with a documented lack of backazimuthal variations in *SKS* splitting that might indicate receiver-side complexity. Although the source-side technique relies on the assumptions of lower mantle isotropy and accurate corrections for receiver-side anisotropy, it has a key advantage in that it samples the subduction system in a way that is complementary to local S measurements. Source-side splitting constrains anisotropy along the downgoing S raypath beneath the earthquake, while local S splitting constrains anisotropy along the upgoing S raypath above the earthquake and *SKS* phases sample the entire upper mantle.

Our measurement strategy closely follows that of *Eakin and Long* [2013] and *Eakin et al.* [2016], who used source-side splitting to constrain deep upper mantle anisotropy beneath the Peruvian flat slab segment, just to the north of our study area. We used eight seismic stations located in North America and Africa in

our analysis (Figure 2), very similar to the set of stations used by *Eakin and Long* [2013]. All of these stations have documented weak upper mantle anisotropy at long periods, such that an explicit correction for anisotropy beneath the station is not needed. Receiver-side splitting for these stations was documented in *Lynner and Long* [2013, 2014], and a detailed description of the assumptions and limitations of the source-side splitting technique can be found in *Lynner and Long* [2013].

We selected large (magnitude greater than 5.8) earthquakes beneath the CAUGHT study region for analysis; a map of events that yielded at least one source-side measurement is shown in Figure 2. Waveforms were bandpass filtered between 0.02 and 1 Hz, as with the teleseismic *SKS* phases examined in this study, with corner frequencies occasionally adjusted slightly for waveform clarity. The shear wave splitting measurement procedure closely followed our approach for local direct *S* phases, with a simultaneous application of the rotation-correlation and the eigenvalue measurement methods, and a determination of measurement quality based on $\phi_{RC} - \phi_{EV}$ and $\delta t_{RC}/\delta t_{EV}$ (Figure 4).

3. Results

3.1. *KS Results

Our measurement procedure yielded a total of 430 well-constrained *KS splitting parameter estimates at the 50 CAUGHT stations, including 78 null measurements and 352 nonnull measurements. Our analysis is hampered somewhat by the relatively limited backazimuthal distribution of seismicity in the epicentral distance range suitable for the analysis of core phases, as indicated by the stereoplots in Figure 5. At most stations, the backazimuthal coverage is quite limited, with most stations only achieving coverage in the southwestern backazimuthal quadrants, and only a few stations achieving coverage in three or more quadrants.

Our *KS measurements are shown in map view in Figure 6; we show a map that includes all measurements as well as one that shows only the highest quality ("good") measurements. This map view reveals significant geographic variability in *KS splitting behavior. CAUGHT stations located in Peru, particularly just to the west and north of Lake Titicaca, exhibit null *KS arrivals over a range of backazimuths, with only a few split arrivals. Those *KS arrivals that are split exhibit considerable scatter in their fast orientations, with many ϕ that are oriented roughly N-S. However, if only the "good" quality measurements are considered (Figure 6b), only a few nonnull measurements with variable fast orientations are present. Beneath southernmost Peru, there is more consistent splitting, with delay times ~1 s and dominantly ESE-WNW fast orientations. Among the northernmost stations in Bolivia, which overlie the portion of the slab that is just downdip of the northernmost Peru stations, we observe fast orientations that are more nearly perpendicular to the slab contours in the deep upper mantle. Along the CAUGHT dense line at stations to the south, we observe significant splitting at nearly all stations, again with average delay times of about 1 s and with fast orientations that trend generally WNW-ESE. These measured ϕ are oblique to subparallel to the strike of the trench along the Peruvian portion of the margin, but the CAUGHT dense line is located near the bend in the trench in the central portion of the South American subduction system (Figure 1, inset), so the trench strike is somewhat difficult to define here. A comparison between the inferred slab contours and the fast *SKS* splitting orientations (Figure 6) reveals that stations along the CAUGHT dense line seem to exhibit fast orientations that are generally parallel or subparallel to the slab strike. Many stations in Bolivia exhibit a number of null *KS arrivals in addition to well-constrained splitting.

A detailed examination of *KS splitting behavior as a function of backazimuth at individual stations, as illustrated in the stereoplots in Figure 5 (blue lines), reveals some evidence for complexity in upper mantle anisotropy beneath our study region. The selection of stations shown in Figure 5 also demonstrates the geographical variations within the CAUGHT array, with a transition from dominantly null splitting and/or N-S fast orientations in the north and west to more nearly E-W splitting in the south and east. At many stations, there is a hint that *KS splitting patterns are not consistent with a single, horizontal layer of anisotropy and instead exhibit complexities such as variations in apparent splitting parameters with backazimuth or a mix of null and split arrivals in certain backazimuthal ranges. We emphasize, however, that the limited backazimuthal coverage means that our *KS data alone cannot definitively distinguish between a single layer of anisotropy and more complicated scenarios.
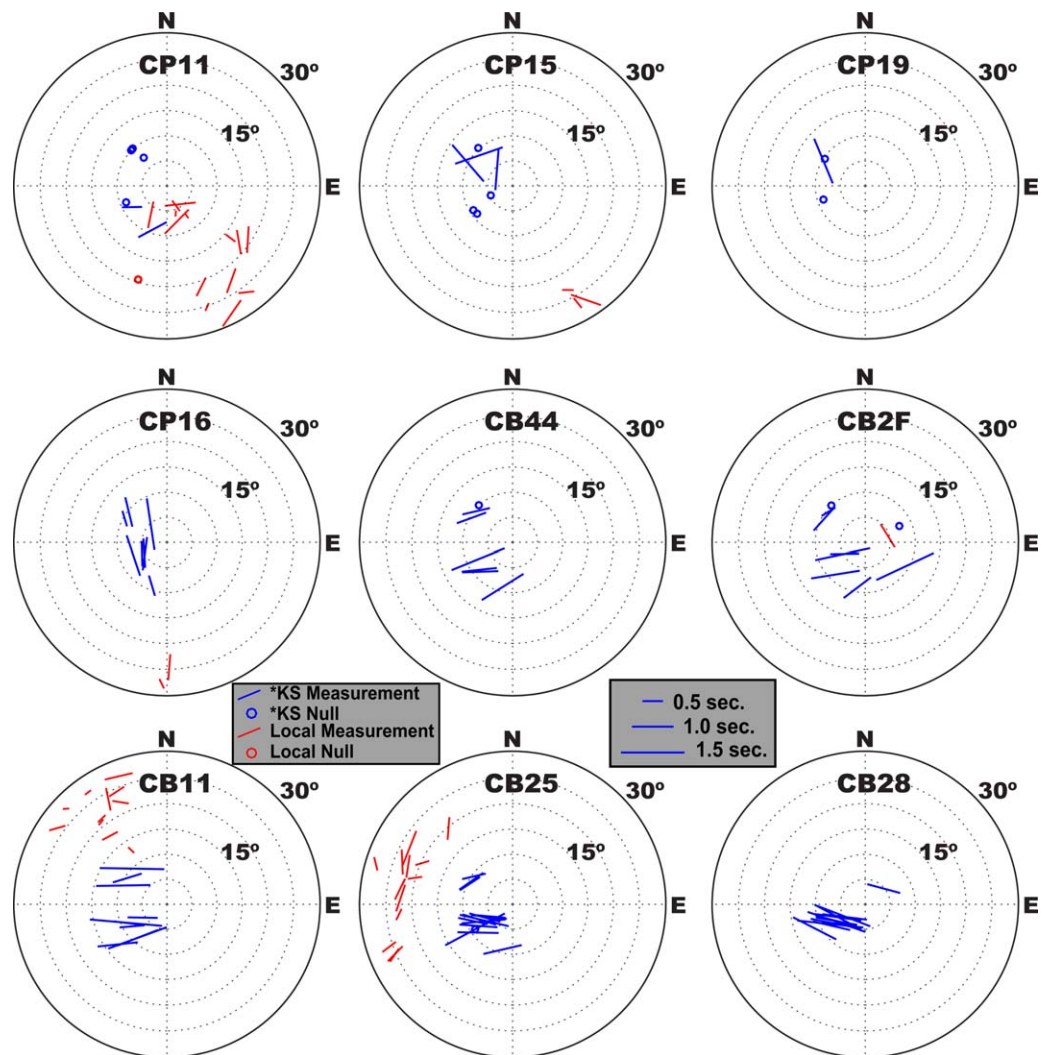
Figure 5. Examples of *KS* (blue) and local S (red) splitting patterns at selected CAUGHT stations. Stereoplots for each station indicate individual measurements plotted as a function of backazimuth (with north at the top of each plot and east at the right) and incidence angle (distance from center; all incidence angles are close to ~10°). Null measurements are indicated with hexagons; split measurements are indicated with bars). Station names are shown at the top of each plot. Stations are arranged roughly in geographical order, with northern stations toward the top of the plot, western stations toward the left, southern stations toward the bottom, and eastern stations toward the right.

3.2. Local S Results

Our local S measurement procedure yielded a total of 636 results, including 4 nulls and 632 split arrivals. These measurements are shown in map view in Figure 7; we also show local S measurements at selected stations on the stereoplots in Figure 5. In contrast to the *KS* data set, we observe a very small number of null arrivals, likely reflecting the much lower delay time detection limit for higher-frequency S waves. We also observe a much larger degree of scatter in the local S measurements compared to *KS*, likely indicating significant heterogeneity in anisotropic structure in the mantle wedge and/or the overriding plate. Along the CAUGHT dense line, we observe a systematic increase in delay times to the north and east that corresponds to a general increase in slab (earthquake) depth, and thus raypath length. Stations located close to the trench show dramatic scatter in measured fast orientations, while stations farther inland exhibit ϕ that are generally parallel to the slab contours. Stations located just to the north and west of the dense line, in southernmost Peru and just to the east of Lake Titicaca, there is a preponderance of generally trench-parallel ϕ, while Peruvian stations located to the west of Lake Titicaca exhibit scattered fast orientations, similar to local S splitting patterns documented at PULSE stations just to the north [Eakin et al., 2014]. A consideration of only "good" quality local S splits reveals very similar patterns, with a slightly reduced number of measurements (Figure 7b).
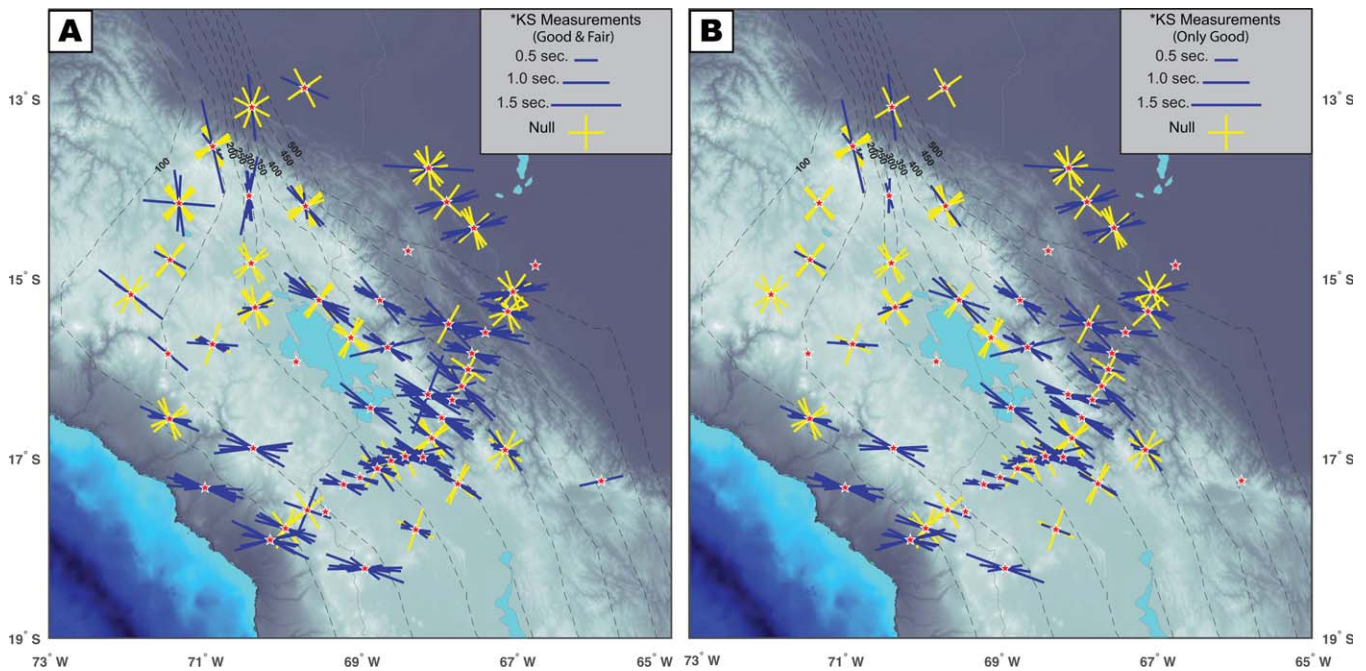
Figure 6. Maps of *KS* splitting measurements. (a) Map of all "good" and "fair" measurements, plotted at the station locations. Blue bars indicate split measurements, with the orientation of the bar corresponding to the fast splitting orientation and its length corresponding to the delay time, as shown in the legend. Null measurements are shown with a yellow cross, with bars oriented parallel to and perpendicular to the event backazimuth, which for *KS* phases correspond to the initial polarization orientation. Slab contours (dashed lines) and CAUGHT station locations (red stars) are shown. Background colors show topography; the large inland body of water in the central portion of the map is Lake Titicaca. (b) Same as Figure 6a, but only "good" quality measurements are shown.
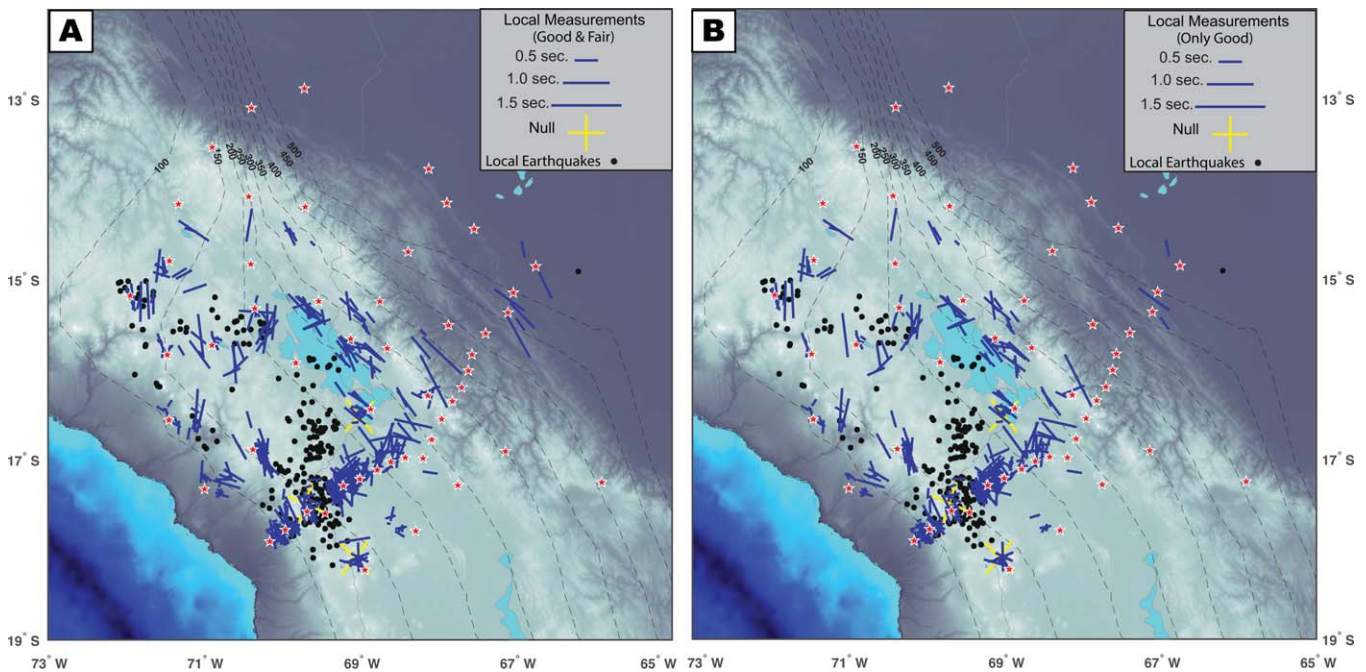

Figure 7. Map of local *S* splitting measurements. (a) Map of all "good" plus "fair" measurements, plotted at the midpoint between the event location (black dots) and the station. (b) Same as Figure 7a, but only "good" quality measurements are shown. Conventions for the plotting of measurements, slab contours, station locations, and topography are as in Figure 6.
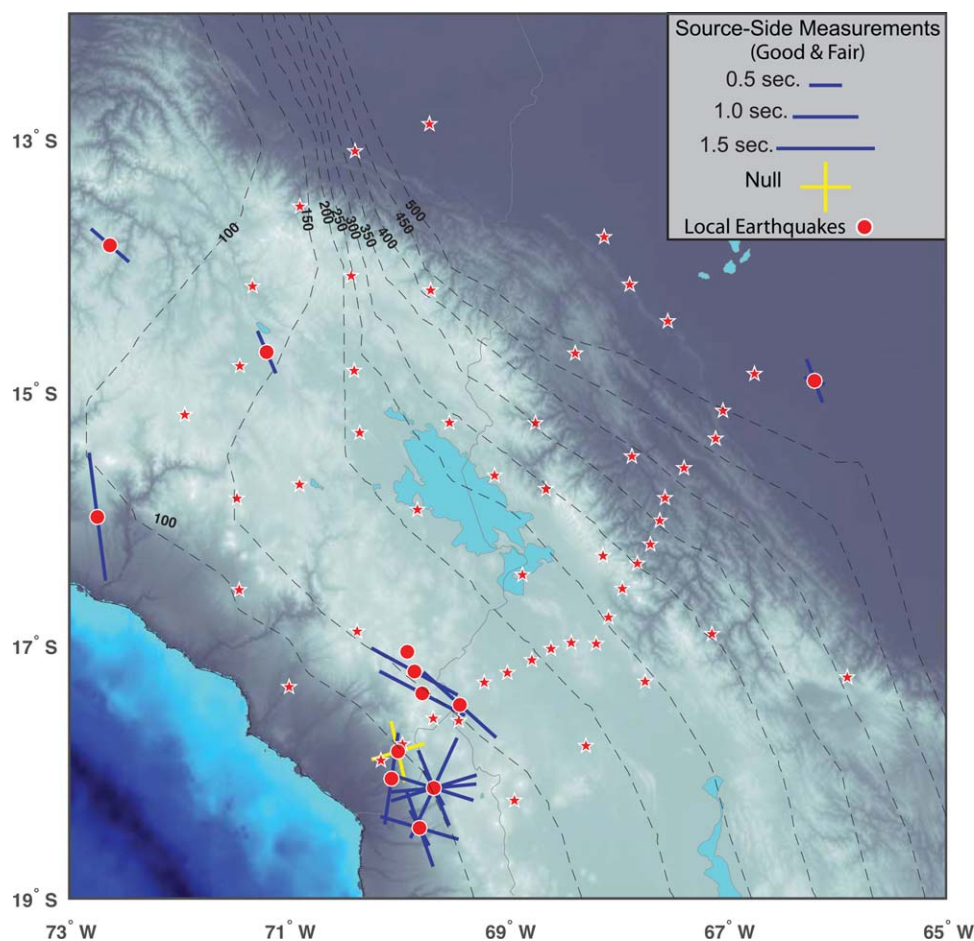
Figure 8. Map of source-side splitting. Split measurements are shown as blue bars, plotted at the earthquake locations. The fast orientations measured at the distant stations have been projected into a ray-centered coordinate system for the downgoing ray by reflecting the fast orientation across a vector representing the backazimuth, as in *Eakin and Long* [2013]. The null measurement is shown with a yellow cross, with the arms oriented parallel and perpendicular to the initial polarization direction, as estimated from the waveform. Topography, slab contours, and station locations are as in Figure 6.

3.3. Source-Side Results

We obtained 20 measurements of source-side splitting from teleseismic direct *S* phases, including one null arrival. Because of the relatively small number of large-magnitude slab events that could be measured teleseismically, and the relatively small number of distant stations beneath which the upper mantle anisotropy is well known and negligibly weak, the source-side data set is considerably smaller than either the *KS* or local *S* data set. Nevertheless, a few spatial patterns are evident, as shown in map view in Figure 8. Beneath southern Peru, fast orientations are generally trench-parallel or subparallel, contrasting somewhat with previously published source-side measurements for this region [*Eakin et al.*, 2016], although the number of measurements in both studies is very small. One deep earthquake beneath the easternmost part of the CAUGHT dense line exhibits about 0.5 s of splitting with trench-parallel ϕ, reflecting anisotropy in the mantle transition zone or uppermost lower mantle similar to that documented by *Lynner and Long* [2015]. Beneath the western portion of the dense line, there is considerable scatter in measured fast orientations, with a group of events exhibiting nearly trench-parallel ϕ and the rest exhibiting no dominant orientation.

4. Discussion

A key advantage of the measurement strategy employed in this study, in which we simultaneously measure the splitting of *KS*, local *S*, and teleseismic direct *S* phases from slab earthquakes, is that it yields a combination of raypaths that sample the subduction system in complementary ways. This is illustrated in Figure 9,
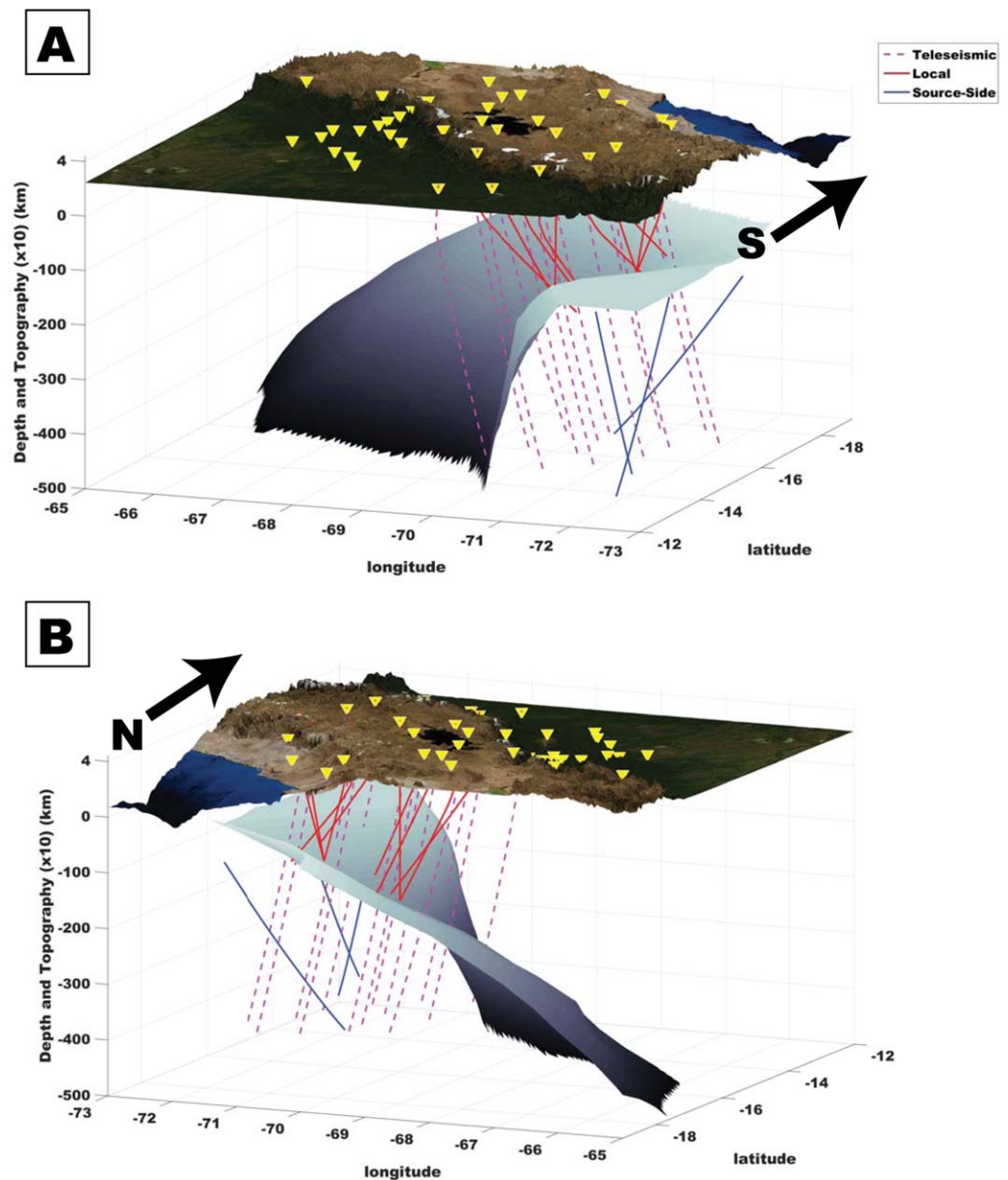
Figure 9. Plot of representative raypaths for the northern group of stations (viewed from the north, a) and the southern group of stations (viewed from the south, b). Surface topography and bathymetry are shown, along with CAUGHT station locations (yellow triangles). Gray surface indicates the top of the slab at depth, from the model of *Scire et al.* [2016]. Dashed pink lines indicate representative *KS raypaths, solid red lines indicate direct local *S*, and solid blue lines indicate source-side teleseismic *S* raypaths. Raypaths were calculated using the TauP traveltime calculator [*Crotwell et al.*, 1999] for the iasp91 velocity model [*Kennett and Engdahl*, 1991].

which shows raypath diagrams for a selection of representative raypaths in our data set. In general, local *S* measurements sample a combination of mantle wedge and overriding plate, the source-side *S* measurements sample a combination of slab and subslab upper mantle, and *KS phases sample all four regions. (Here we make the common assumption that upper mantle anisotropy is responsible for the splitting of *KS phases, with little or no contribution from the lower mantle. This has been shown to be generally true on a global scale [e.g., *Niu and Perez*, 2004; *Becker et al.*, 2012], although there are regional exceptions [e.g., *He and Long*, 2011; *Long and Lynner*, 2015].)

The raypath diagrams in Figure 9 illustrate that the relative contributions from different portions of the subduction systems vary with station location, which gives us an opportunity to use the data set as a whole to constrain the likely relative contributions. For example, the local *S* raypaths, when viewed from the south

(Figure 9b), demonstrate that stations close to the trench likely sample a relatively large portion of overriding plate (crustal thickness values here range up to ~65 km [*Beck and Zandt*, 2002]) and only a relatively small (perhaps 30–50 km) portion of mantle wedge material. In contrast, local *S* phases from deep earthquakes measured at stations far inland have much larger paths in the mantle wedge (up to ~300 km). Similarly, the complex slab morphology at depth evident in Figure 9 implies that some *KS* phases (e.g., those measured at inland stations in the northern portion of the array; Figure 9a) sample mostly the steeply dipping portion of the subducting slab in the deeper part of the upper mantle, while others (stations located closer to the trench) sample a relatively larger portion of the subslab upper mantle.

With these raypath configurations in mind, we can carry out a comparison of splitting parameters among different phases and stations (Figures 5 and 10) to understand the relative contributions from different portions of the subduction system. Beneath the northwestern portion of the array (Figure 10a), we observe very similar average fast orientations for local *S* and *KS* phases, with average delay times that are somewhat higher for *KS* (~ 0.8 s) than local *S* (~ 0.4 s). In this portion of the study area, the source-side *S* measurements are not perfectly collocated with the CAUGHT stations, so a direct comparison is difficult. At the one source-side event located within the CAUGHT footprint, the measured delay time is intermediate between local *S* and *SKS* averages and the fast orientation is different by ~30°–50°, but this comparison is based on a single measurement.

Beneath the southern and eastern portion of the array (Figure 10b), which includes the dense line, the superior station coverage allows us to discern robust geographic trends. At stations located close to the trench (leftmost third of the plots in Figure 10b), the local *S* and *KS* phases exhibit very similar average fast orientations but substantially different average delay times (~0.25 s for local *S*, while *KS* delay times decrease from over 1 to ~0.7 s). This suggests that *KS* phases are sampling substantial anisotropy within the subslab mantle; this inference is borne out by a comparison to the source-side *S* measurements, which exhibit similar fast orientations and slightly higher delay times. Moving to the middle portion of the southern stations, local *S* delay times increase slightly as path lengths through the mantle wedge increase. Furthermore, measured ϕ values are substantially different than stations near the trench and exhibit a systematic rotation with increasing sampling of the mantle wedge, perhaps suggesting complex and spatially variable anisotropy within the wedge. In contrast, *KS* splitting parameters remain relatively constant across the array, particularly the measured fast orientations. There is, however, a slight increase in *KS* delay times across the central portion of the array that is similar to the increase in local *S* delay times, although the *KS* δt values are higher. For stations located farthest away from the trench (right third of the plots in Figure 10b), the differences between *KS* and local *S* splitting parameters are modest, suggesting that both phases are sampling mostly anisotropy in the mantle wedge. Measured *KS* delay times are systematically slightly higher than those obtained from local *S* phases, suggesting that either there is a small contribution from anisotropy in the deep upper mantle or that the observed splitting parameters have a dependence on the frequency content of the waves [e.g., *Marson-Pidgeon and Savage*, 1997; *Eakin and Long*, 2013].

These comparisons, which are more straightforward for stations in the southern portion of the array, allow us to draw some first-order conclusions about the geometry and strength of anisotropy in different portions of the subduction system. The maximum contribution from anisotropy in the overriding plate is constrained by the local *S* splitting behavior at stations located close to the trench, which mostly sample the overriding plate and which exhibit splitting delay times of ~0.25 s. This relatively modest inferred contribution from anisotropy in the crust and mantle lithosphere in the overriding plate is notable, given the thick crust (up to ~65 km) and the fact that the overriding plate has undergone substantial deformation and shortening in order to build the high topography [e.g., *Garzione et al.*, 2008]. The small delay times that we attribute to the overriding plate beneath the CAUGHT study area imply that anisotropy in the wedge, slab, and subslab mantle makes the primary contribution to the *KS* splitting observations, which exhibit average delay times of ~ 1 s. Interestingly, our inference that the overriding plate makes only a small contribution to the observed splitting contrasts with inferences made elsewhere in the Central Andean Plateau. Specifically, *Wölbern et al.* [2014] argued that relatively strong anisotropy in the crust (~4.5%) makes a major contribution to patterns of *KS* and local *S* splitting at a latitude of ~21°S, beneath the central portion of the plateau. Unfortunately, there are few independent constraints on inherited crustal fabrics in these regions that might shed additional light on this difference, but this represents an important target for future research.
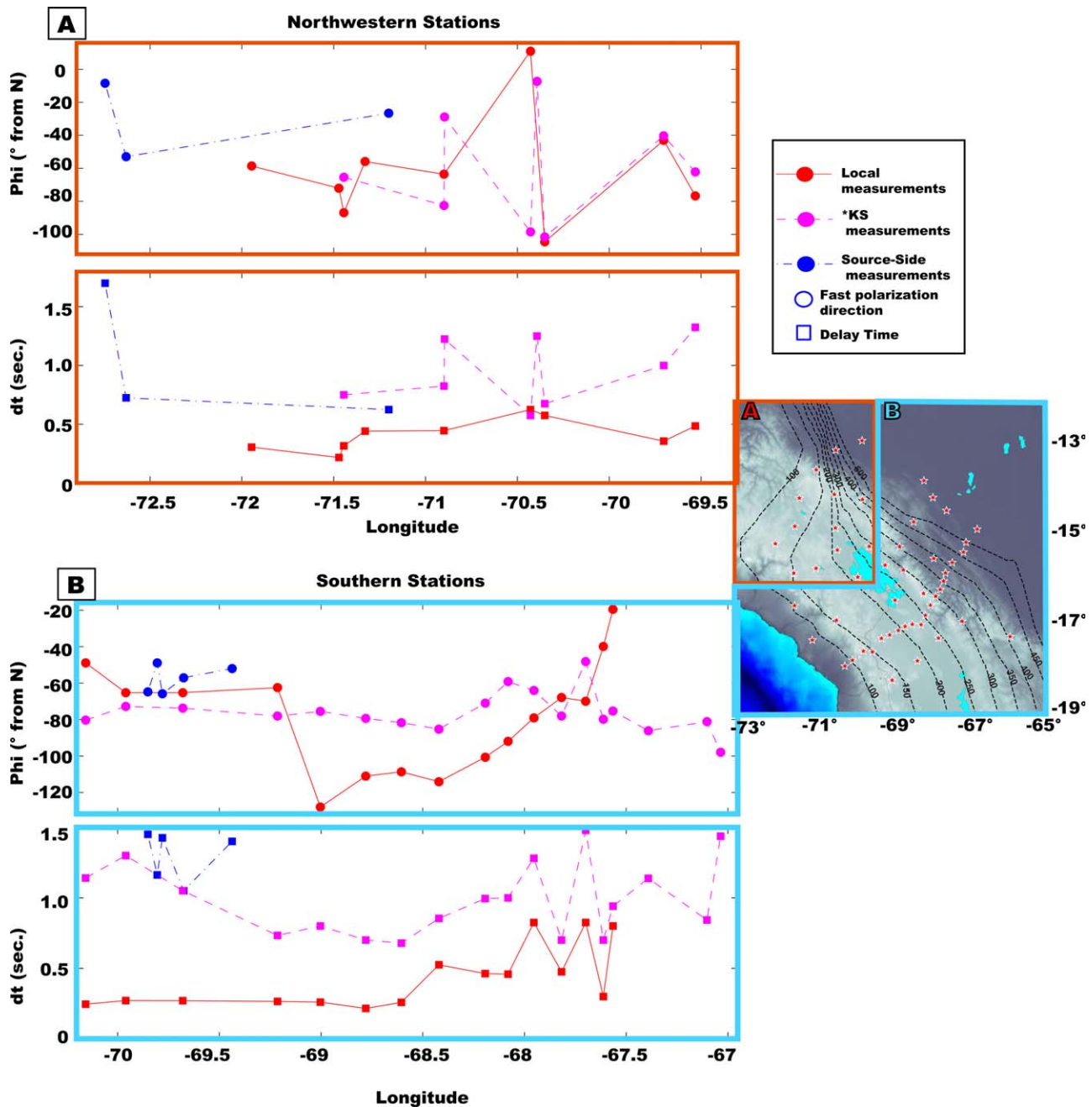
Figure 10. Comparison of station-averaged shear wave splitting parameters measured for different phases for (a) northwestern and (b) southern groups. (top plots) Average measured fast orientations (degrees from N), (bottom plots) Average measured delay times (s), each plotted as a function of station longitude (*KS and local S), or event longitude (source side S). *KS measurements are shown in pink, local S measurements are shown in red, and source-side S measurements are shown in blue. Inset shows geographic distribution of stations in each group. (The few stations located to the east of −67° longitude did not yield enough results to be included on the plot, so Figure 10a is cut off at −67°.)

The observable increase in local *S* delay times across the CAUGHT dense line (Figure 10b) provides evidence for a contribution from mantle wedge anisotropy beneath the array. However, several lines of evidence suggest that the pattern of wedge anisotropy is likely to be complex, including the large amount of scatter in the measured fast orientations evident in map view (Figure 7) and the relatively weak average bulk anisotropy suggested by the modest delay times (~0.8 s) exhibited by phases originating from relatively deep earthquakes that have long path lengths in the wedge (~300 km). Our interpretation of wedge anisotropy is further complicated by the possibility of unusual olivine fabric types or the presence of serpentinite minerals, which can modify the usual relationships between strain and anisotropy. In particular, B-type olivine

fabric may be present in the relatively cold, high-stress forearc portion of the wedge [e.g., *Kneller et al.*, 2005], and strongly anisotropic serpentinite minerals may also be present in the relatively cold portions of the wedge [e.g., *Katayama et al.*, 2009; *Jung*, 2011; *McCormack et al.*, 2013; *Wagner et al.*, 2013].

Despite these potential complexities, a few conclusions about the geometry of flow in the wedge can be drawn based on map views of our results (Figures 6 and 7) as well as comparisons among splitting patterns observed for different types of phases in this study (Figures 5 and 10). A group of stations located in the backarc, particularly the stations located just to the east of Lake Titicaca, exhibit local *S* fast orientations that are generally parallel to the underlying slab contours (Figure 7). Because these raypaths sample a portion of the mantle wedge where B-type olivine fabric and serpentinite minerals are unlikely to be present, these measurements provide clear evidence for a departure from simple two-dimensional corner flow. An along-strike component to mantle wedge flow may be induced here by the complex morphology of the flat slab segment just to the north [e.g., *Kneller and van Keken*, 2007, 2008], or by a combination of trench migration, slab rollback, and background mantle flow [e.g., *Hoernle et al.*, 2007; *Long and Wirth*, 2013]. Intriguingly, there is a suggestion from the **KS* splitting patterns at the northernmost stations in Bolivia (Figure 6) that there may be a transition in the wedge flow pattern in the very far backarc. These stations overlie the slab at transition zone depths, so the *SKS* phases mainly sample wedge anisotropy with no contribution from the slab or subslab mantle, and here the fast orientations are more nearly perpendicular to the slab contours, in contrast to stations located closer to the trench. It is worth noting, however, that local *S* measurements from deep events at the eastern end of the CAUGHT dense array just to the south, although sparse, mostly exhibit ϕ that are nearly parallel to the slab contours (Figure 7).

At stations beneath the arc and forearc regions, we observe average fast orientations that are generally nearly trench-parallel (Figure 10b), but individual measurements display considerable scatter (Figure 7). In this region, the relationships between wedge flow and anisotropy are ambiguous, but the degree of scatter in the local *S* measurements suggests a complex wedge flow regime, again perhaps due to the complex slab morphology to the north [e.g., *Eakin et al.*, 2014]. Another intriguing, although speculative, possibility is that the wedge flow here is complex due to recent lithospheric delamination at the base of the overriding plate [e.g., *DeCelles et al.*, 2009; *Scire et al.*, 2016], which may have produced a complex, time-dependent mantle wedge flow field [e.g., *Behn et al.*, 2007; *West et al.*, 2009].

Beneath the slab, our observations also provide evidence for a significant departure from the classical model of simple, two-dimensional entrained mantle flow beneath subducting slabs. Source-side *S* measurements, along with **KS* measurements from stations located relatively close to the trench, provide fairly direct sampling of the subslab mantle; while these phases also sample the downgoing slab itself, in regions with a shallow or normal slab dip the path lengths in the slab itself are generally shorter than in the subslab mantle [e.g., *Long*, 2013]. Both types of phases (Figures 6 and 8) provide evidence for fast orientations in the subslab mantle that are parallel or subparallel to the trench strike, suggesting that there is a significant component of along-strike flow in the subslab mantle. A reasonable estimate of the possible thickness of an anisotropic subslab layer, based on an average V_S of 4.7 km/s, a nominal anisotropic strength of 4%, and our average observed source-side delay time of 1.05 s, yields roughly 130 km; if the anisotropic strength is lower, the required layer thickness would be greater, and vice versa. The idea that slab rollback might induce toroidal flow with a significant along-strike component beneath subducting slabs was first proposed for South America by *Russo and Silver* [1994], and subsequent studies have argued that many subduction systems exhibit such flow [e.g., *Peyton et al.*, 2001; *Civello and Margheriti*, 2004; *Zandt and Humphreys*, 2008; *Long and Silver*, 2008; *Faccenda and Capitanio*, 2013; *Lynner and Long*, 2013]. It should be noted, however, that (nearly) trench-parallel fast splitting orientations beneath subducting slabs are not ubiquitous [e.g., *Lynner and Long*, 2014], and alternative explanations for trench-parallel ϕ in the subslab mantle have also been proposed [*Song and Kawakatsu*, 2012].

Contributions to shear wave splitting observations from anisotropy within the slab itself are typically difficult to discern, as the portions of raypaths (particularly for **KS*) that sample the slab are usually short compared to the portions sampling other regions of the subduction system. There is, however, evidence for a contribution from the slab itself to some of the **KS* measurements presented in this study. We focus in particular on the small number of stations in the northern part of the CAUGHT array that exhibit nearly N-S fast orientations, in contrast to the generally E-W fast orientations observed elsewhere. Recent work by *Eakin et al.* [2016] used local *S* splitting data measured at stations of the PULSE array, just to the north and west of CAUGHT, along with source-side *S* measurements, to infer relatively strong anisotropy in the subducting Nazca slab in the deep upper mantle ($\sim$200–400 km) with fast orientations parallel to the slab strike. We
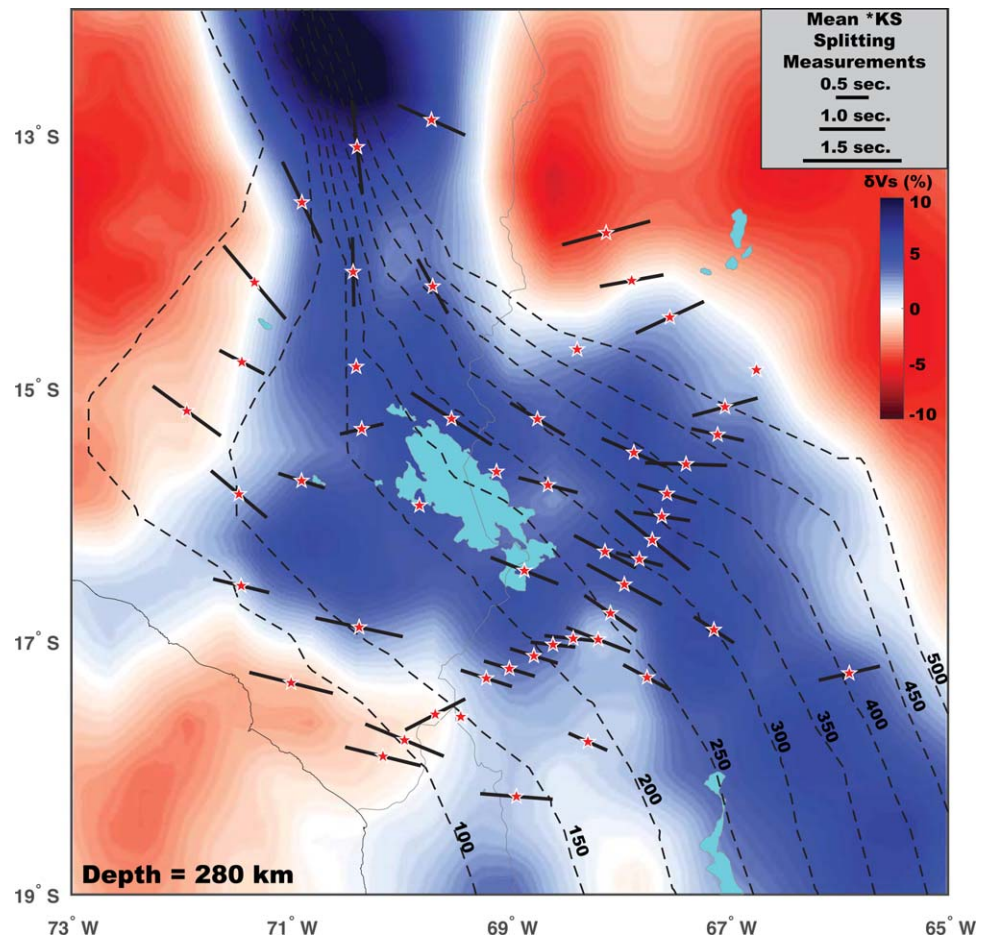
Figure 11. Single-station averaged *KS* splitting measurements plotted on top of an upper mantle shear velocity model. Splitting parameters are plotted at the station location. Background colors show upper mantle *S* velocities at a depth of 280 km from *Scire et al.* [2016].

propose that this slab anisotropy signal extends to the south, to the steeply dipping portion of the slab beneath the northern stations of CAUGHT, and that this slab anisotropy accounts for the N-S *KS* fast orientations observed there. The steep dip of the slab beneath these stations means that *KS* rays with near vertical incidence spend a considerable amount of their time in upper mantle traveling through the slab (Figure 9). The geometry of the subducting Nazca slab in the deep upper mantle has recently been constrained via body wave tomography by *Scire et al.* [2016]; a comparison between the slab geometry in the upper mantle and our average *KS* splitting observations (Figure 11) suggests the possibility that additional CAUGHT stations that exhibit ϕ parallel to the slab contours may also reflect a contribution from slab anisotropy.

A more general comparison between the shear wave splitting measurements presented here and those made at the PULSE array to the north and west is instructive; taken together, these data sets reflect the along-strike transition from flat to normally dipping subduction. Figure 12 shows the measurements made in this study, along with measurements made for the same types of phases (*KS*, local *S*, source-side *S*) beneath the PULSE study area from *Eakin and Long* [2013] and *Eakin et al.* [2014, 2015, 2016]. The first-order aspects of the splitting patterns for *KS* and local *S* phases, in particular, are not strikingly different between the southern portion of the flat slab segment and the northern portion of the normally dipping segment. However, taken together the two data sets delineate an intriguing feature: there is a region that encompasses the central portion of the PULSE southern line, along with the CAUGHT stations just to the west of Lake Titicaca, that is dominated by mostly null *KS* arrivals, with a few split *KS* measurements with relatively small δt and highly scattered ϕ. This type of regionally pervasive, dominantly null *KS* splitting pattern has not been observed elsewhere in the South American subduction system. This feature was previously described by *Eakin et al.* [2015], although they could not constrain its southern extent; in combination with the CAUGHT splitting data set, it is clear that this region of dominantly null *KS* arrivals coincides geographically with the
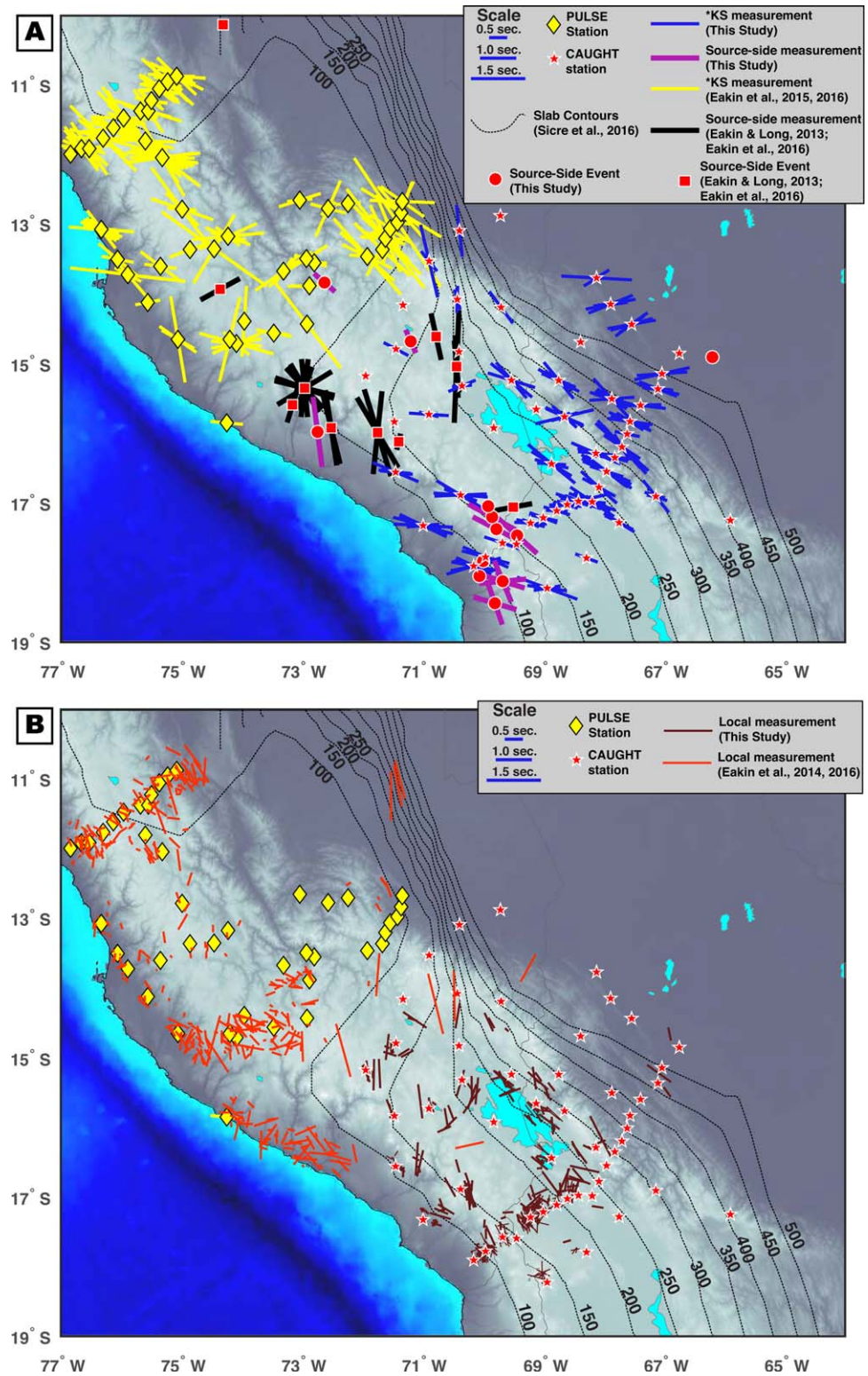
Figure 12. Comparison between shear wave splitting measurements in this study and measurements just to the north beneath the Peru flat slab segment, from *Eakin and Long* [2013] and *Eakin et al.* [2014, 2015, 2016]. We show *KS* and source-side *S* measurements (a) as well as local *S* measurements (b) for both the PULSE and CAUGHT arrays.
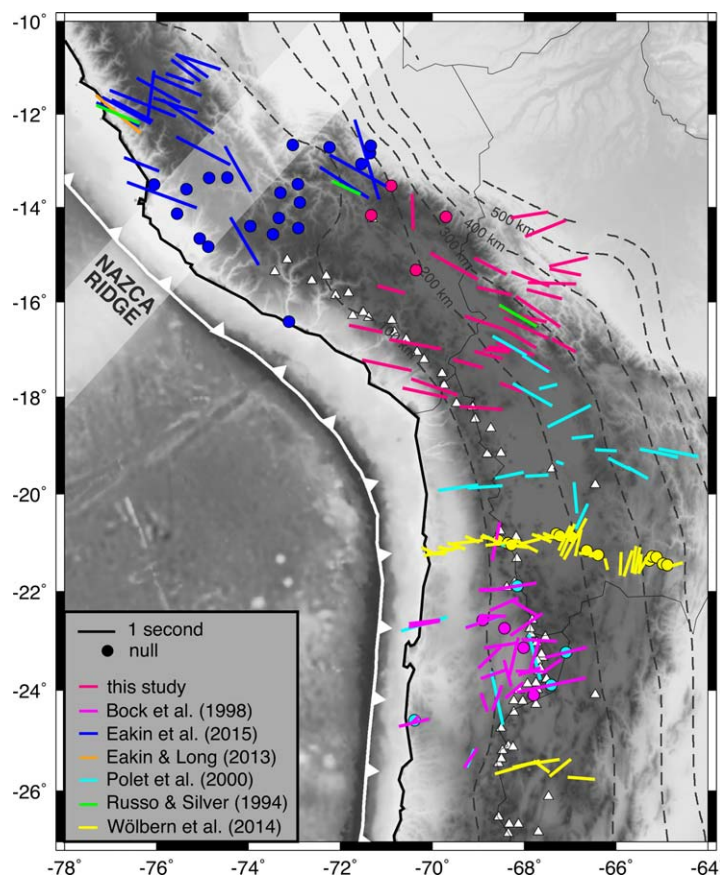
Figure 13. Compilation of *SKS* (and other core phase) splitting measurements along the western boundary of South America between 10° and 27°S. Slab contours (dashed lines) are from the Slab1.0 model of *Hayes et al.* [2012]. Single-station average *SKS* splitting parameters from the literature are shown plotted at station locations. For CAUGHT and PULSE stations, we calculated **KS* average splitting parameters for all stations with at least four measurements. Circles indicate stations with dominantly null arrivals, with at least four null arrivals and no more than three split measurements.

along-strike transition from flat to normally dipping subduction. *Eakin et al.* [2015] articulated several possible explanations for this feature, including highly heterogeneous anisotropy in the overriding plate and/or wedge mantle that obscures the signal from deeper mantle anisotropy, or the possibility of a nearly vertical axis of anisotropic symmetry that results in weak or absent azimuthal anisotropy. Future studies using data from the CAUGHT and PULSE arrays that seek to characterize radial anisotropy (i.e., velocity differences between vertically and horizontally polarized waves) may help to further constrain the origin of this feature.

Zooming out to an even larger regional scale, the CAUGHT shear wave splitting data set fills in what had been a notable gap in geographical coverage for published splitting studies for core phases in the central portion of the South American subduction zone. Taken as a whole, *SKS* (and other core phase) measurements along the western edge of South America reveal significant complexity (Figure 13). To the north of the concave bend in Andean topography, *SKS* fast splitting orientations are generally trench-parallel, with the previously discussed region of dominantly null *SKS* arrivals near the transition from flat to normally dipping subduction. Near the bend and to its south, *SKS* splitting patterns are substantially more complicated, with many stations exhibiting more nearly trench-perpendicular ϕ, and much more lateral variability in general. Early observations of trench-parallel ϕ along the South American subduction zone motivated the hypothesis of widespread toroidal subslab flow due to slab rollback beneath the Nazca slab [*Russo and Silver*, 1994], which has long served as a working hypothesis for this subduction system. As demonstrated in Figure 13, the vastly improved coverage since the work of *Russo and Silver* [1994] shows that *SKS* splitting observations from the western margin of South America are substantially more complex than might be expected from the toroidal flow model. We emphasize, however, that because *SKS* splitting generally reflects anisotropy not just in the subslab mantle, but also in the slab, wedge, and overriding plate, caution is needed when interpreting *SKS* fast splitting orientations in terms of mantle flow, and complementary constraints from other seismic phases (local *S*, source-side teleseismic *S*) are critical. Furthermore, the generally poor backazimuthal coverage available for **KS* splitting studies in South America limits our availability to interpret them as straightforward indicators of mantle flow. For example, *Eakin and Long* [2013] argued that frequency-dependent *SKS* splitting beneath station NNA in Peru, with generally nearly trench-parallel ϕ, may be consistent with multiple layers of anisotropy, including a deep layer (perhaps beneath the slab) that is nearly perpendicular to the trench. In general, the substantial complexity in the compilation of *SKS* splitting parameters for the central part of the South American subduction zone (Figure 13) challenges some aspects of the *Russo and Silver* [1994] subslab flow model, and highlights the utility of combining

constraints from direct *S* phases with *SKS* splitting measurements to constrain anisotropy in different portions of the subduction system.

5. Summary

We have examined the splitting of shear waves that sample the upper mantle beneath the northern portion of the Central Andean Plateau in southern Peru and northern Bolivia. Our analysis strategy combines different types of seismic phases, including core-traversing phases such as *SKS* and both local and teleseismic *S* waves that originate from earthquakes within the subducting Nazca slab. This combination of phases that sample different portions of the subduction system allow us place some constraints on the contributions from seismic anisotropy in the overriding plate, mantle wedge, subducting slab, and subslab mantle. We document splitting patterns that are complex and variable in our study region. There is a group of stations in the north that exhibit mostly null **KS* arrivals, consistent with previous studies above the southernmost portion of the Peruvian flat slab, and likely indicating significant lithospheric heterogeneity. A group of stations with **KS* paths that mostly sample the Nazca slab show distinctive slab-parallel fast orientations, while those that mostly sample the subslab region appear mostly trench-parallel to oblique, inconsistent with the predictions for simple 2-D entrained flow. These observations are consistent with inferences on subslab anisotropy from source-side teleseismic *S* splitting. Local *S* measurements show more scatter and somewhat smaller delay times, with a trend of increasing δt with increasing distance from the trench, arguing for a significant contribution from anisotropy within the mantle wedge and only a small contribution from the overriding plate. Our inference of relatively weak overriding plate anisotropy contrasts with observations that suggest strong crustal anisotropy elsewhere in the Central Andean Plateau, and may suggest lateral variability in crustal deformation within this region of high topography. Observations of trench-parallel fast orientations for local *S* phases that sample the backarc mantle wedge argue for a departure from simple two-dimensional corner flow. Overall, our data set suggests that a complex mix of processes affect the anisotropic structure of the subduction system beneath the Central Andean Plateau, possibly including slab-driven flow, rollback-induced along-strike flow, lithospheric delamination, and deformation of the slab in the deep upper mantle.

References

Anderson, M. L., G. Zandt, E. Triep, M. Fouch, and S. Beck (2004), Anisotropy and mantle flow in the Chile-Argentina subduction zone from shear wave splitting analysis, *Geophys. Res. Lett.*, *31*, L23608, doi:10.1029/2004GL020906.

Antonijevic, S. K., L. S. Wagner, A. Kumar, S. L. Beck, M. D. Long, G. Zandt, H. Tavera, and C. Condori (2015), The role of ridges in the formation and longevity of flat slabs, *Nature*, *524*, 212–215, doi:10.1038/nature14648.

Beck, S. L., and G. Zandt (2002), The nature of orogenic crust in the central Andes, *J. Geophys. Res.*, *107*(B10), 2230, doi:10.1029/2000JB000124.

Becker, T. W., S. Lebedev, and M. D. Long (2012), On the relationship between azimuthal anisotropy from shear wave splitting and surface wave tomography, *J. Geophys. Res.*, *117*, B01306, doi:10.1029/2011JB008705.

Behn, M. D., G. Hirth, and P. B. Kelemen (2007), Trench-parallel anisotropy produced by foundering of arc lower crust, *Science 317*, 108–111, doi:10.1126/science.1141269.

Bilek, S. (2010), Seismicity along the South American subduction zone: Review of large earthquakes, tsunamis, and subduction zone complexity, *Tectonophysics*, *495*, 2–14, doi:10.1016/j.tecto.2009.02.037.

Bock, G., R. Kind, A. Rudloff, and G. Asch (1998), Shear wave anisotropy in the upper mantle beneath the Nazca plate in northern Chile, *J. Geophys. Res.*, *103*, 24,333–24,345.

Cahill, T., and B.L. Isacks (1992), Seismicity and shape of the subducted Nazca Plate, *J. Geophys. Res.*, *97*, 17,503–17,529.

Civello, S., and L. Margheriti (2004), Toroidal mantle flow around the Calabrian slab (Italy) from SKS splitting, *Geophys. Res. Lett.*, *31*, L10601, doi:10.1029/2004GL019607.

Crotwell, H. P., T. J. Owens, and J. Ritsema (1999), the TauP Toolkit: Flexible seismic travel-time and ray-path utilities, *Seismol. Res. Lett.*, *70*, 154–160.

DeCelles, P. G., M. N. Ducea, P. Kapp, and G. Zandt (2009), Cyclicity in Cordilleran orogenic systems, *Nat. Geosci.*, *2*, 251–257, doi:10.1038/ngeo469.

Di Leo, J., A. Walker, Z.-H. Li, J. Wookey, N. Ribe, J.-M. Kendall, and A. Tommasi (2014), Development of texture and seismic anisotropy during the onset of subduction, *Geochem. Geophys. Geosyst.*, *15*, 192–212, doi:10.1002/2013GC005032.

Eakin, C. M., and M. D. Long (2013), Complex anisotropy beneath the Peruvian flat slab from frequency-dependent, multiple-phase shear wave splitting analysis, *J. Geophys. Res. Solid Earth*, *118*, 4794–4813, doi:10.1002/jgrb.50349.

Eakin, C. M., M. D. Long, S. L. Beck, L. S. Wagner, H. Tavera, and C. Condori (2014), Response of the mantle to flat slab evolution: Insights from local S splitting beneath Peru, *Geophys. Res. Lett.*, *41*, 3438–3446, doi:10.1002/2014GL059943.

Eakin, C. M., M. D. Long, L. S. Wagner, S. L. Beck, and H. Tavera (2015), Upper mantle anisotropy beneath Peru from *SKS* splitting: Constraints on flat slab dynamics and interaction with the Nazca Ridge, *Earth Planet. Sci. Lett.*, *412*, 152–162, doi:10.1016/j.epsl.2014.12.015.

Eakin, C. M., M. D. Long, A. Scire, S. L. Beck, L. S. Wagner, G. Zandt, and H. Tavera (2016), Internal deformation of the subducted Nazca slab inferred from seismic anisotropy, *Nat. Geosci.*, *9*, 56–59, doi:10.1038/ngeo2592.

Faccenda, M., and F. A. Capitanio (2013), Seismic anisotropy around subduction zones: Insights from three-dimensional modeling of upper mantle deformation and SKS splitting calculations, *Geochem. Geophys. Geosyst.*, *14*, 243–262, doi:10.1002/ggge.20055.

Garzione, C. N., G. D. Hoke, J. C. Libarkin, S. Withirs, B. MacFadden, J. Eiler, P. Ghosh, and A. Mulch (2008), Rise of the Andes, *Science*, *320*, 1304–1307, doi:10.1126/science.1148615.

Gripp, A. E., and R. G. Gordon (2002), Young tracks of hotspots and current plate velocities, *Geophys. J. Int.*, *150*, 321–361, doi:10.1046/j.1365-246X.2002.01627.x.

Hampel, A. (2002), The migration history of the Nazca Ridge along the Peruvian active margin: A re- evaluation, *Earth Planet. Sci. Lett.*, *203*, 665–679.

Hayes, G. P., D. J. Wald, and R. L. Johnson (2012), Slab1.0: A three-dimensional model of global subduction zone geometries, *J. Geophys. Res.*, *117*, B01302, doi:10.1029/2011JB008524.

He, X., and M. D. Long (2011), Lowermost mantle anisotropy beneath the northwestern Pacific: Evidence from PcS, ScS, SKS, and SKKS phases, *Geochem. Geophys. Geosyst.*, *12*, Q12012, doi:10.1029/2011GC003779.

Heuret, A., and S. Lallemand (2005), Plate motions, slab dynamics and back-arc deformation, *Phys. Earth Planet. Inter.*, *149*, 31–51, doi:10.1016/j.pepi.2004.08.022.

Hicks, S. P., S. E. J. Nippress, and A. Rietbrock (2012), Sub-slab mantle anisotropy beneath south-central Chile, *Earth Planet. Sci. Lett.*, *357–358*, 203–213, doi:10.1016/j.epsl.2012.09.017.

Hoernle, K., et al. (2007), Arc-parallel flow in the mantle wedge beneath Costa Rica and Nicaragua, *Nature*, *451*, 1094–1097, doi:10.1038/nature06550.

Jung, H. (2011), Seismic anisotropy produced by serpentine in mantle wedge, *Earth Planet. Sci. Lett.*, *307*, 535–543, doi:10.1016/j.epsl.2011.05.041.

Katayama, I., K. Hirauchi, K. Michibayashi, and J. Ando (2009), Trench-parallel anisotropy produced by serpentine deformation in the hydrated mantle wedge, *Nature*, *461*, 1114–1117. doi:10.1038/nature08513.

Kennett, B. L. N., and E. R. Engdahl (1991), Traveltimes for global earthquake location and phase identification, *Geophys. J. Int.*, *105*, 104, 429–465, doi:10.1111/j.1365-246X.1991.tb06724.x.

Kneller, E. A., and P. E. van Keken (2007), Trench-parallel flow and seismic anisotropy in the Marianas and Andean subduction systems, *Nature*, *450*, 1222–1225, doi:10.1038/nature06429.

Kneller, E. A., and P. E. van Keken (2008), Effect of three-dimensional slab geometry on deformation in the mantle wedge: Implications for shear wave anisotropy, *Geochem. Geophys. Geosyst.*, *9*, Q01003, doi:10.1029/2007GC001677.

Kneller E. A., P. E. van Keken, S. Karato and J. Park (2005), B-type olivine fabric in the mantle wedge: Insights from high- resolution non-Newtonian subduction zone models, *Earth Planet. Sci. Lett.*, *237*, 781–797.

Kumar, A., L. S. Wagner, S. L. Beck, M. D. Long, G. Zandt, B. Young, H. Tavera, and E. Minaya (2016), Seismicity and state of stress in the central and southern Peruvian flat slab, *Earth Planet. Sci. Lett.*, *441*, 71–80, doi:10.1016/j.epsl.2016.02.023.

Lamb, S., and L. Hoke (1997), Origin of the high plateau in the Central Andes, Bolivia, South America, *Tectonics*, *16*, 623–649.

Long, M. D. (2013), Constraints on subduction geodynamics from seismic anisotropy, *Rev. Geophys.*, *51*, 76–112, doi:10.1002/rog.20008.

Long, M. D., and C. Lynner (2015), Seismic anisotropy in the lowermost mantle near the Perm Anomaly, *Geophys. Res. Lett.*, *42*, 7073–7080, doi:10.1002/2015GL065506.

Long, M. D., and P. G. Silver (2008), The subduction zone flow field from seismic anisotropy: A global view, *Science*, *319*, 315–318.

Long, M. D., and E. A. Wirth (2013), Mantle flow in subduction systems: The mantle wedge flow field and implications for wedge processes, *J. Geophys. Res. Solid Earth*, *118*, 583–606, doi:10.1002/jgrb.50063.

Lynner, C., and M. D. Long (2013), Sub-slab seismic anisotropy and mantle flow beneath the Caribbean and Scotia subduction zones: Effects of slab morphology and kinematics, *Earth Planet. Sci. Lett.*, *361*, 367–378.

Lynner, C., and M. D. Long (2014), Sub-slab seismic anisotropy beneath the Sumatra and circum-Pacific subduction zones from source-side shear wave splitting observations, *Geochem. Geophys. Geosyst.*, *15*, 2262–2281, doi:10.1002/2014GC005239.

Lynner, C., and M. D. Long (2015), Heterogeneous seismic anisotropy in the transition zone and uppermost lower mantle: Evidence from South America, Izu-Bonin and Japan, *Geophys. J. Int.*, *201*, 1545–1552, doi:10.1093/gji/ggv099.

MacDougall, J. G., K. M. Fischer, and M. L. Anderson (2012), Seismic anisotropy above and below the subducting Nazca lithosphere in southern South America, *J. Geophys. Res.*, *117*, B12306, doi:10.1029/2012JB009538.

Marson-Pidgeon, K., and M. K. Savage (1997), Frequency dependent anisotropy in Wellington, New Zealand, *Geophys. Res. Lett. 24*, 3297–3300.

McCormack, K., E. A. Wirth, and M. D. Long (2013), B-type olivine fabric and mantle wedge serpentinization beneath the Ryukyu arc, *Geophys. Res. Lett.*, *40*, 1697–1702, doi:10.1002/grl.50369.

Niu, F., and A. M. Perez (2004), Seismic anisotropy in the lower mantle: A comparison of waveform splitting of *SKS* and *SKKS*, *Geophys. Res. Lett.*, *31*, L24612, doi:10.1029/2004GL021196.

Peyton, V., V. Levin, J. Park, M. Brandon, J. Lees, E. Gordeev, and A. Ozerov (2001), Mantle flow at a slab edge: Seismic anisotropy in the Kamchatka region, *Geophys. Res. Lett.*, *28*, 379–382, doi:10.1029/2000GL012200.

Phillips, K., and R. W. Clayton (2014), Structure of the subduction transition region from seismic array data in southern Peru, *Geophys. J. Int.*, *196*, 1889–1905, doi:10.1093/gji/ggt504.

Polet, J., P. G. Silver, S. Beck, T. Wallace, G. Zandt, S. Rupper, R. Kind, and A. Rudloff (2000), Shear wave anisotropy beneath the Andes from the BANJO, SEDA, and PISCO experiments, *J. Geophys. Res.*, *105*, 6287–6304.

Porritt, R. W., T. W. Becker, and G. Monsalve (2014), Seismic anisotropy and slab dynamics from SKS splitting recorded in Colombia, *Geophys. Res. Lett.*, *41*, 8775–8783, doi:10.1002/2014GL061958.

Ramos, V. A. and A. Folguera (2009), Andean flat-slab subduction through time, in *Ancient Orogens and Modern Analogues*, edited by J. B. Murphy, J. D. Keppie, and A. J. Hynes, *Geol. Soc. Spec. Publ.*, 327, 31–54.

Rosenbaum, G., D. Giles, M. Saxon, P. G. Betts, R. F. Weinberg, and C. Duboz (2005), Subduction of the Nazca Ridge and the Inca Plateau: Insights into the formation of ore deposits in Peru, *Earth Planet. Sci. Lett.*, *239*, 18–32.

Russo, R. M. (2009), Subducted oceanic asthenosphere and upper mantle flow beneath the Juan de Fuca slab, *Lithosphere*, *1*, 195–205.

Russo, R. M., and P. G. Silver (1994), Trench-parallel flow beneath the Nazca Plate from seismic anisotropy, *Science*, *263*, 1105–1111.

Savage, M. K. (1999), Seismic anisotropy and mantle deformation: What have we learned from shear wave splitting?, *Rev. Geophys.*, *37*, 65–106.

Schellart, W. P., D. R. Stegman, and J. Freeman (2008), Global trench migration velocities and slab migration induced upper mantle volume fluxes: Constraints to find an Earth reference frame based on minimizing viscous dissipation, *Earth Sci. Rev.*, *88*, 118–144, doi:10.1016/j.earscirev.2008.01.005.

Scire, A., G. Zandt, S. Beck, M. Long, L. Wagner, E. Minaya, and H. Tavera (2016), Imaging the transition from flat to normal subduction: Variations in the structure of the Nazca slab and upper mantle under southern Peru and northwestern Bolivia, *Geophys. J. Int.*, *204*, 457–479, doi:10.1093/gji/ggv452.

Silver, P. G., and W. W. Chan (1991), Shear wave splitting and subcontinental mantle deformation. *J. Geophys. Res.*, *96*, 16,429–16,454.

Song, T.-R. A., and H. Kawakatsu (2012), Subduction of oceanic asthenosphere: Evidence from sub-slab seismic anisotropy, *Geophys. Res. Lett.*, *39*, L17301, doi:10.1029/2012GL052639.

Strecker, M. R., R. N. Alonso, B. Bookhagen, B. Carrapa, G. E. Hilley, E. R. Sobel, and M. H. Trauth (2007), Tectonics and climate of the Southern Central Andes, *Annu. Rev. Earth Planet. Sci.*, *35*, 747–787, doi:10.1146/annurev.earth.35.031306.140158.

Syracuse, E. M., and G. A. Abers (2006), Global compilation of variations in slab depth beneath arc volcanoes and implications, *Geochem. Geophys. Geosyst.*, *7*, Q05017, doi:10.1029/2005GC001045.

Wagner, L. S., M. J. Fouch, D. E. James, and M. D. Long (2013), The role of hydrous phases in the formation of trench parallel anisotropy: Evidence from Rayleigh waves in Cascadia, *Geophys. Res. Lett.*, *40*, 2642–2646, doi:10.1002/grl.50525.

West, J. D., M. J. Fouch, J. B. Roth, and L. T. Elkins-Tanton (2009), Vertical mantle flow associated with a lithospheric drip beneath the Great Basin, *Nat. Geosci.*, *2*, 439–444, doi:10.1038/ngeo526.

Wölbern, I., U. Löbl, and G. Rümpker (2014), Crustal origin of trench-parallel shear-wave fast polarizations in the Central Andes, *Earth Planet. Sci. Lett. 392*, 230–238, doi:10.1016/j.epsl.2014.02.032

Wüstefeld, A., and G. Bokelmann (2007), Null detection in shear-wave splitting measurements, *Bull. Seismol. Soc. Am.*, *97*, 1204–1211.

Wüstefeld, A., G. Bokelmann, C. Zaroli, and G. Barruol (2008), SplitLab: A shear-wave splitting environment in Matlab, *Comput. Geosci.*, *34*, 515–528.

Zandt, G., and E. Humphreys (2008), Toroidal mantle flow through the western U.S. slab window, *Geology*, *36*, 295–298, doi:10.1130/G24611A.1.